Electronic States in Zinc Magnesium Oxide Alloy Semiconductors: Hard X-ray Photoemission Spectroscopy and Density Functional Theory Calculations

Takeo Ohsawa,[†,‡] Yutaka Adachi,[§,||] Isao Sakaguchi,[§,||] Kenji Matsumoto,[†,⊥] Hajime Haneda,[†,⊥] Shigenori Ueda,[#] Hideki Yoshikawa,[#] Keisuke Kobayashi,[#] and Naoki Ohashi*[,§,||,⊥]

International Center for Materials Nanoarchitectonics (MANA), Optronic Materials Center, and Sensor Materials Center, National Institute for Materials Science (NIMS), 1-1 Namiki, Tsukuba, Ibaraki 305-0044, Japan, Department of Applied Science for Electronics and Materials (ASEM), Kyushu University, 6-1 Kasuga Koen, Kasuga, Fukuoka 816-8580, Japan, and NIMS Beamline Station at SPring-8, 1-1-1 Kouto, Sayo-cho, Sayo-gun, Hyogo 679-5148, Japan

Received September 11, 2008. Revised Manuscript Received November 12, 2008

The electronic states of zinc magnesium oxide $(Zn_{1-x}Mg_x)O$ thin films were determined exactly by hard X-ray photoemission spectroscopy (HX-PES) using synchrotron radiation. The Zn 2p core level was shifted to a higher binding energy along with widening of the bandgap by alloying with MgO, whereas the shift of the O 1s peak was less than that of the Zn 2p peak. Density functional theory (DFT) calculations revealed that the electronic state of an O ion bonding with an adjacent Mg ion is remarkably different from that not bonding with a Mg ion. As a result, the energy shift observed in the O 1s peak results from a combination of the expansion of the bandgap energy and the chemical shift due to a change in the ionicity. The Fermi level is always situated just below the conduction band; this suggests that a shallow donor can be added, even in the alloy film with very high MgO fraction, for example, $x = 0.47$.

Introduction

Metal-oxide semiconductors exhibit various electronic, dielectric, and optical functionalities. Zinc oxide (ZnO), remarkably, is an excellent oxide semiconductor material for device applications such as transparent electrodes,[1] surface acoustic wave (SAW) devices,[2] and ultraviolet LEDs.[3−7] A wide-gap alloy material with lattice constants that are close to those of wurtzite ZnO is essential to employ ZnO as an active channel in heterojunction devices. To gain more fundamental insight into ZnO-based alloy semiconductors, intensive studies on the ZnO−MgO pseudobinary system have shed light on bandgap engineering for wurtzite ZnO grown by several methods ranging from magnetron sputtering[8,9] and metalorganic chemical vapor deposition[10,11] to pulsed-laser deposition,[12−17] indicating the ability to tune the band structure, exceptionally useful to tailor the performance of optoelectronic devices.[17−20] Indeed, it has been known that the bandgap energy (E_g) of ZnO can be tuned from 3.3 to 4.5 eV by forming $(Zn_{1-x}Mg_x)O$ satisfying Vegard's law in the wurtzite phase.[12−14] Recently, very thick (≈0.5 mm) $(Zn_{1-x}Mg_x)O$ alloy films with 2 in. diameters have been

* To whom correspondence should be addressed. E-mail: ohashi.naoki@nims.go.jp.
† Sensor Materials Center, National Institute for Materials Science.
‡ Present address: Pacific Northwest National Laboratory, WA, USA.
§ International Center for Materials Nanoarchitectonics, National Institute for Materials Science.
|| Optronic Materials Center, National Institute for Materials Science.
⊥ Kyushu University.
NIMS Beamline Station at SPring-8.

(1) Minami, T. *Semicond. Sci. Technol.* **2005**, *20*, S35.
(2) Nakahata, H.; Higaki, K.; Hachigo, A.; Shikata, S.; Fujimori, N.; Takahashi, Y.; Kajihara, T.; Yamamoto, Y. *Jpn. J. Appl. Phys.* **1994**, *33*, 324.
(3) Tsukazaki, A.; Onuma, T.; Ohtani, M.; Makino, T.; Sumiya, M.; Ohtani, K.; Chichibu, S. F.; Fuke, S.; Segawa, Y.; Ohno, H.; Koinuma, H.; Kawasaki, M. *Nat. Mater.* **2005**, *4*, 42.
(4) Tsukazaki, A.; Kubota, M.; Ohtomo, A.; Onuma, T.; Ohtani, K.; Ohno, H.; Chichibu, S. F.; Kawasaki, M. *Jpn. J. Appl. Phys.* **2005**, *44*, L643.
(5) Wei, Z. P.; Lu, Y. M.; Shen, D. Z.; Zhang, Z. Z.; Yao, B.; Li, B. H.; Zhang, J. Y.; Zhao, D. X.; Fan, X. W.; Tang, Z. K. *Appl. Phys. Lett.* **2007**, *90*, 042113.
(6) Xu, W. Z.; Ye, Z. Z.; Zeng, Y. J.; Zhu, L. P.; Zhao, B. H.; Jiang, L.; Lu, J. G.; He, H. P.; Zhang, S. B. *Appl. Phys. Lett.* **2006**, *88*, 173506.
(7) Nakamura, A.; Ohashi, T.; Yamamoto, K.; Ishihara, J.; Aoki, T.; Temmyo, J.; Gotoh, H. *Appl. Phys. Lett.* **2007**, *90*, 093512.
(8) Fang, G.-J.; Li, D.; Zhao, X. *Phys. Status Solidi A* **2003**, *200*, 361.
(9) Kang, J. H.; Park, Y. R.; Kim, K. J. *Solid State Commun.* **2000**, *115*, 127.
(10) Kim, C.; Leem, S.-J.; Robinson, I. K.; Park, W. I.; Kim, D. H.; Yi, G.-C. *Phys. Rev. B* **2002**, *66*, 113404.
(11) Ku, C.-H.; Chiang, H.-H.; Wu, J.-J. *Chem. Phys. Lett.* **2005**, *404*, 132.
(12) Ohtomo, A.; Kawasaki, M.; Koida, T.; Masubuchi, K.; Koinuma, H. *Appl. Phys. Lett.* **1998**, *72*, 2466.
(13) Ohtomo, A.; Tsukazaki, A. *Semicond. Sci. Technol.* **2005**, *20*, S1.
(14) *Thin Films and Heterostructures for Oxide Electronics*; Ogale, S. B., Ed.; Springer: New York, 2005.
(15) Ryoken, H.; Ohashi, N.; Sakaguchi, I.; Adachi, Y.; Hishita, S.; Haneda, H. *J. Cryst. Growth* **2006**, *287*, 134.
(16) Sharma, A. K.; Narayan, J.; Muth, J. F.; Teng, C. W.; Jin, C.; Kvit, A.; Kolbas, R. M.; Holland, O. W. *Appl. Phys. Lett.* **1999**, *75*, 3327.
(17) Sasa, S.; Ozaki, M.; Koike, K.; Yano, M.; Inoue, M. *Appl. Phys. Lett.* **2006**, *89*, 053502.
(18) Tampo, H.; Matsubara, K.; Yamada, A.; Shibata, H.; Fons, P.; Yamagata, M.; Kanie, H.; Niki, S. *J. Cryst. Growth* **2007**, *301/302*, 358.
(19) Jo, J.; Seo, O.; Choi, H.; Lee, B. *Appl. Phys. Express* **2008**, *1*, 041202.
(20) Tsukazaki, A.; Yuji, H.; Akasaka, S.; Tamura, K.; Nakahara, K.; Tanabe, T.; Takasu, H.; Ohtomo, A.; Kawasaki, M. *Appl. Phys. Express* **2008**, *1*, 055004.

10.1021/cm802467n CCC: $40.75
Published on Web 12/12/2008

grown by a liquid phase epitaxy technique.[21] This suggests significant potential for developing transparent electronics and LEDs for practical applications.

Numerous reports notwithstanding, the electronic state in $(Zn_{1-x}Mg_x)O$ is still in question despite its significance for utilizing the ZnO/$(Zn_{1-x}Mg_x)O$ heterostructure for transparent device applications. Knowledge of Fermi level pinning is an important issue for the fabrication of junction devices, and charge compensation has to be investigated for developing a doping technology for $(Zn_{1-x}Mg_x)O$ alloys. A number of tools have been employed to investigate electronic structures of condensed matter. Photoemission spectroscopy (PES) is a powerful experimental technique to characterize the electronic structure of a material, enabling direct observation of electron density of states (DOS). Conventional PES using an X-ray source of Mg Kα (1253.6 eV) or Al Kα (1486.6 eV) is typically a *surface*-sensitive technique (∼1 nm) due to the short inelastic mean free path of photoelectrons in solids. This means that surface contamination, such as adsorption of water molecules, makes it difficult to characterize the bulk electronic state using conventional PES. In contrast, hard X-ray photoemission spectroscopy (HX-PES) used in this study can realize a large escape depth (5−10 nm) of high kinetic energy photoelectrons (∼6 keV), thereby allowing the elucidation of *bulk*-sensitive electronic states.[22−25] Very recently, we reported our HX-PES results on $(Zn_{1-x}Mg_x)O$ alloys with varying MgO fraction (x).[25] The Fermi level (E_F) of the alloy was found to be close to the conduction band minimum (CBM) even in the film with $x = 0.47$. This is good news, since it suggests that the formation of shallow donor states is possible even in alloys with high MgO fractions.

Here, we report the striking features of the electronic states in $(Zn_{1-x}Mg_x)O$ alloy films as determined by HX-PES and electronic structure calculations using density functional theory (DFT). The shift of the HX-PES peaks with the MgO fraction will be discussed in relation to the results of DFT calculations.

Experimental Section

$(Zn_{1-x}Mg_x)O$ alloy thin films were grown on yttria-stabilized cubic zirconia (YSZ) (111) substrates by pulsed-laser deposition (PLD). The fourth harmonic generation of a Nd:YAG laser (λ = 266 nm)[15,25] with a repetition rate of 1 Hz was employed for ablation of MgO-containing ZnO targets. The growth temperature and the oxygen pressure were held constant at 700 °C and 1.5×10^{-5} Torr, respectively. We also grew epitaxial $(Zn_{1-x}Mg_x)O$ films on single-crystalline ZnO substrates to examine the effects of crystallite size and the presence of grain boundaries on HX-PES spectra.

X-ray diffraction (XRD) and atomic force microscopy (AFM) were employed to characterize the film structures and morphologies, respectively. The electronic properties of the films were determined by means of Hall effect measurements, and the E_g of the obtained alloy films was determined from optical transmittance measurements. MgO fractions in the films were obtained using secondary ion mass spectroscopy (SIMS) and were assigned by the calibration curve for standard samples.[15]

HX-PES measurements were performed at the undulator beamline, BL15XU, of the SPring-8 facility. HX-PES spectra were taken at room temperature using a Scienta R4000 electron energy analyzer with a total energy resolution of about 255 meV, as verified with Fermi edge measurement for pure gold. The excitation energy was fixed at 5.95 keV, and the estimated inelastic mean free paths of the photoelectrons ranged between 5 and 10 nm. The takeoff angle of the photoelectrons measured from the surface of the samples was set to 80−85 to reduce the effect of surface contamination on the HX-PES spectra. In this study, we examined the HX-PES results of $(Zn_{1-x}Mg_x)O$ with $x = 0.0$, 0.07,and 0.47.

Theoretical Simulation. In DFT calculations, we constructed superlattice models as model structures of the alloy compound, and their electronic structures were calculated using the CASTEP code.[26] The superlattice models consist of $2 \times 2 \times 1$, $\sqrt{3} \times \sqrt{3} \times 1$, $\sqrt{3} \times \sqrt{3} \times 2$, $2 \times 2 \times 2$, and $3 \times 3 \times 2$ times unit cells of wurtzite-type ZnO, and one or a few Mg atoms were substituted for Zn atoms in the supercell. The highest Mg concentration in the supercell model was $[Zn_6Mg_2O_8]$ in the $2 \times 2 \times 1$ supercell, and the lowest one was $[Zn_{47}MgO_{48}]$ in the $2\sqrt{3} \times 2\sqrt{3} \times 2$ supercell. Typical superlattice models are displayed in the next section.

The pseudopotential approach using an ultrasoft potential[27] was employed, and a generalized gradient approximation (GGA)[28] was selected as the exchange correlation function. The number of k-points involved in the Brillouin zone (BZ) integrations and the cutoff energy for the electronic band structure calculation were varied to examine the convergence of the calculated total energy values. The k-points for BZ integration were selected according to the report by Monkhorst and Pack,[29,30] and the cutoff energy was set to 380 eV for the results shown below. We used the pseudopotentials given in Materials Studio version 3.1, which was commercially available from Accelrys Software Inc., San Diego, CA, USA. Self-consistent total energy mineralization was done using the density mixing method.[31] The crystalline structure, including both lattice parameters and internal atomic coordinates, was optimized by the BFGS algorithm[32] using the results of the DFT calculation. We assumed that the supercell should have C_{3v} symmetry even after structural relaxation and this was only constrained for the structural optimization. The convergent tolerances for electronic state optimization were set to 5.0×10^{-7} eV/atom, and those for structural optimization were set to 0.1 eV/nm for maximum interatomic force, 0.02 GPa for residual stress, and 5.0×10^{-5} nm for maximum atomic displacement.

Since we employed an ultrasoft pseudopotential approach for computational economy, the electronic state of core-levels, such

(21) Kobayashi, J.; Sekiwa, H.; Miyamoto, M.; Ohashi, N.; Sakaguchi, I.; Wada, Y.; Adachi, Y.; Haneda, H. *Appl. Phys. Express* **2008**, *1*, 071201.
(22) Kobayashi, K.; Yabashi, M.; Takata, Y.; Tokushima, T.; Shin, S.; Tamasaku, K.; Miwa, D.; Ishikawa, T.; Nohira, H.; Hattori, T.; Sugita, Y.; Nakatsuka, O.; Sakai, A.; Zaima, S. *Appl. Phys. Lett.* **2003**, *83*, 1005.
(23) Kobayashi, K. *Nucl. Instrum. Methods, Sect. A* **2005**, *547*, 98, and references therein.
(24) Takata, Y.; Tamasaku, K.; Tokushima, T.; Miwa, D.; Shin, S.; Ishikawa, T.; Yabashi, M.; Kobayashi, K.; Kim, J. J.; Yao, T.; Yamamoto, T.; Arita, M.; Namatame, H.; Taniguchi, M. *Appl. Phys. Lett.* **2004**, *84*, 4310.
(25) Ohsawa, T.; Ohashi, N.; Adachi, Y.; Sakaguchi, I.; Ryoken, H.; Matsumoto, K.; Haneda, H.; Ueda, S.; Yoshikawa, H.; Kobayashi, K. *Appl. Phys. Lett.* **2008**, *92*, 232108.
(26) Segall, M. D.; Lindan, P. J. D.; Probert, M. J.; Pickard, C. J.; Hasnip, P. J.; Clark, S.; Payne, M. C. *J. Phys.: Condens. Matter* **2002**, *14*, 2717.
(27) Vanderbilt, D. *Phys. Rev. B* **1990**, *41*, 7892.
(28) Perdew, J. P.; Chevary, J. A.; Vosko, S. H.; Jackson, K. A.; Pederson, M. R.; Singh, D. J.; Fiolhais, C. *Phys. Rev. B* **1992**, *46*, 6671.
(29) Monkhorst, H. J.; Pack, J. D. *Phys. Rev. B* **1976**, *13*, 5188.
(30) Monkhorst, H. J.; Pack, J. D. *Phys. Rev. B* **1977**, *16*, 1748.
(31) Kresse, G.; Furthmuller, J. *Phys. Rev. B* **1996**, *54*, 11169.
(32) Fischer, T. H.; Almlof, J. *J. Phys. Chem.* **1992**, *96*, 9768.

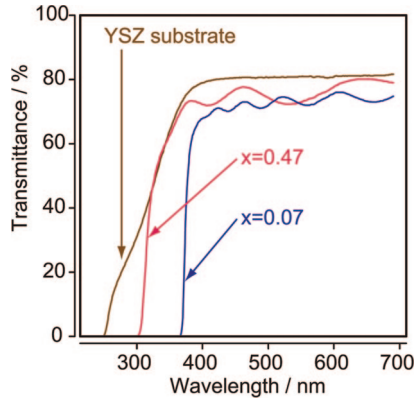

Figure 1. Optical transmittance spectra in $(Zn_{1-x}Mg_x)O$ films grown on YSZ substrates.

as Zn 2p and O 1s, was not involved in the electronic structure simulation. All-electron techniques, such as the WIEN2k code,[33] were not available in this study. Thus, we focused on the calculated local density of state (L-DOS) for the O 2s level and effective ionic charge (Mulliken charges)[34,35] of each atom to elucidate the chemical shift of the HX-PES peaks by alloying with MgO.

Results and Discussion

All the as-grown films were *c*-axis-oriented wurtzite-type $(Zn_{1-x}Mg_x)O$, and the *c*-axis length decreased when x increased, as revealed by XRD measurements.[15] This indicates that Mg ions were evidently incorporated into the ZnO lattice to form a wurtzite-type $(Zn_{1-x}Mg_x)O$ alloy. Figure 1 shows the typical optical transmittance spectra of the $(Zn_{1-x}Mg_x)O$ films. This indicates expansion of E_g when x increases. The value of E_g deduced from transmittance spectra for the as-grown film with $x = 0.47$ was ~4 eV, which was 0.7 eV larger than that of pure ZnO. E_g of the other samples with different x were also estimated and are discussed later in relation to the change in PES peaks.

Figure 2a shows the O 1s peaks in $(Zn_{1-x}Mg_x)O$ films with different x grown on YSZ substrates. From these results, we found that there are three kinds of changes in the HX-PES profile induced by alloying. The first feature is that the O 1s peak in Figure 2a consists of two peaks. We named one the "main peak", found in the E_B range of 531−532 eV. The other, denoted as the "subpeak" in the figure, was a shoulder-like peak in the E_B range of 532~533 eV. The second feature is the shift of the main O 1s peak to the higher E_B side when x increases in the film. In addition to these two features, the width of the main O 1s peaks increased with increasing x. Actually, the peak width for the film with $x = 0.47$ was wider than that of the film with $x = 0.0$ and 0.07. We will further discuss these spectroscopic features below.

We first discuss the origin of the subpeaks in the O 1s core levels. Figure 2b compares the O 1s peak for the $(Zn_{1-x}Mg_x)O$ film grown on ZnO with that on the YSZ substrate. Note that the MgO fractions in both films are close

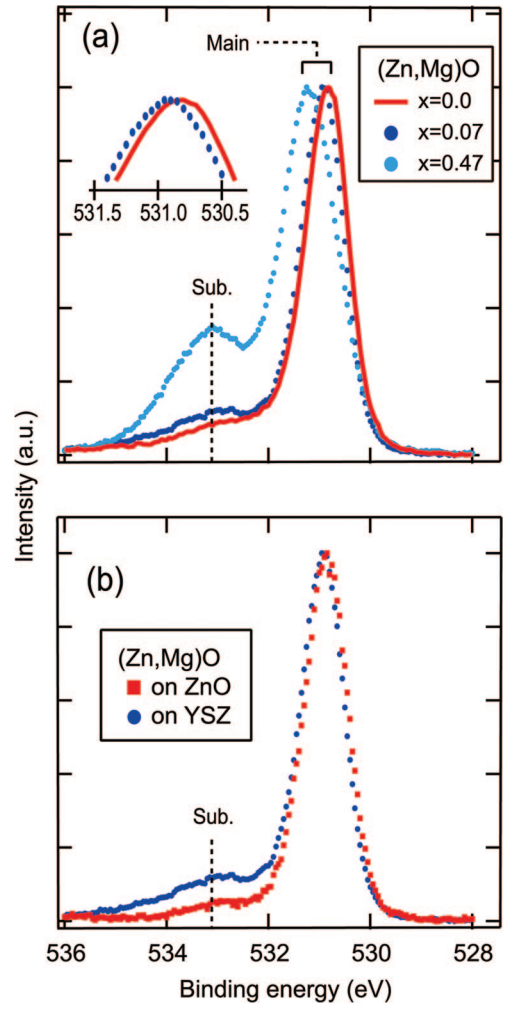

Figure 2. Hard X-ray photoemission (HX-PES) spectra in the O 1s region for as-grown $(Zn_{1-x}Mg_x)O$ films $x = 0.0$, 0.07, and 0.47, on the YSZ substrate (a) and the films on the ZnO and YSZ substrates (b). Inset in (a) shows an enlarged plot for $x = 0.0$ and 0.07. See text for notation of "Main" and "Sub".

to each other. It is evident that the intensity of the subpeak was reduced in the spectrum for the $(Zn_{1-x}Mg_x)O$ film grown on ZnO compared to that on YSZ, implying that the appearance of a subpeak at the higher E_B side was not solely due to alloying. In terms of surface morphologies of these films obtained using AFM, the film on the YSZ substrate showed a granular morphology, while that on the ZnO substrate had a smooth surface. These results suggest that the subpeak became intense when the films had a granular structure. Since an intense subpeak was observed in pure ZnO films having a granular structure and a mosaic structure (not shown), it is evident that the intensity of the subpeak was strongly affected by morphology. One may claim that the subpeak was O ions at the regular surface of (Zn,Mg)O or at low-coordinated sites, because the subpeak was rather abundant in the samples with small grains. The binding energy of the subpeak should depend on x if the subpeak originates from oxygen at the topmost surface having a dangling bond, because some of surface oxygens must have an Mg−O bond. From these reasons, we concluded that the subpeak originated from molecules or ions, such as O_2^-, OH^-, and CO_3^{2-}, adsorbed at grain boundaries and/or dislocations. Since grain boundaries lie perpendicular to the

(33) Schwarz, K.; Blaha, P.; Madsen, G. K. H. *Comput. Phys. Commun.* **2002**, *147*, 71.
(34) Segall, M. D.; Pickard, C. J.; Shah, R.; Payne, M. C. *Mol. Phys.* **1996**, *89*, 571.
(35) Segall, M. D.; Shah, R.; Pickard, C. J.; Payne, M. C. *Phys. Rev. B* **1996**, *54*, 16317.

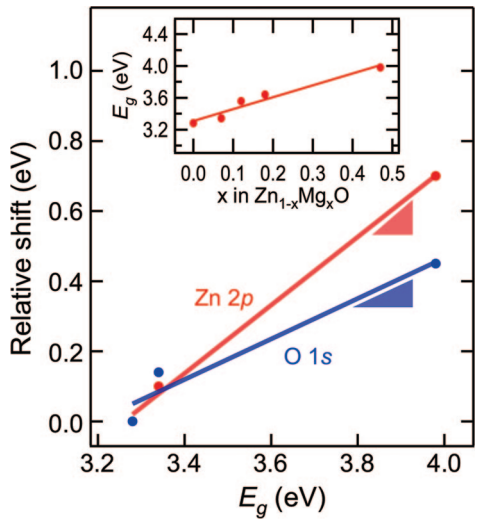

Figure 3. Relative peak shifts in Zn 2p and O 1s peaks plotted as a function of the optical bandgap (E_g) in $(Zn_{1-x}Mg_x)O$. The inset shows the MgO fraction (x) dependence of E_g of the as-grown wurtzite $(Zn_{1-x}Mg_x)O$ films.

surface, these adsorbates can be obviously observed despite the use of *bulk*-sensitive HX-PES.

According to the paper by Erhart et al.,[36] it appears that *p*-type ZnO favors an interstitial oxygen forming dumbbell-like coordination. However, the films used in this study exhibited *n*-type conductivity, as judged by Hall effect measurements. Assuming that an interstitial oxygen is incorporated into our films, an interstitial Zn (Zn_i) or oxygen vacancy (V_O) must coexist in the film to show *n*-type conductivity. If a high concentration of Zn_i or V_O exists with a high concentration of interstitial oxygen, there should be a change in the shapes of the Zn 2p peaks, simultaneous with the O 1s peak. However, there were almost no changes observed in the Zn 2p peaks when x was varied.[25] Moreover, the value of E_B for the subpeak was independent of x, showing that the chemical state of oxygen that causes the subpeak was independent of $(Zn_{1-x}Mg_x)O$. Thus, we concluded that interstitial oxygen is not the origin of the appearance of the subpeak in the O 1s spectra.

Returning to the energy shift of the main O 1s peak with increasing x in $(Zn_{1-x}Mg_x)O$, the main peak tends to shift to the higher E_B side as x increases. Actually, an obvious peak shift (~0.4 eV) was found in the spectrum for the film with $x = 0.47$ compared to the E_B for $x = 0.0$. The energy shift for $x = 0.07$ was very small but evidently seen (~0.15 eV) as shown in the inset in Figure 2a, and the peak shift toward higher E_B with increasing x was also observed in the films grown on the ZnO substrate, as shown in Figure 2b. Thus, we can conclude that the O 1s peak shifted systematically with x in the alloy films.

As reported in our previous study,[25] not only the O 1s peak but also the Zn 2p peak showed a shift to the higher E_B side with increasing x. Figure 3 summarizes the relative shifts (ΔE) of the Zn 2p and the O 1s peaks plotted as a function of E_g in $(Zn_{1-x}Mg_x)O$. Here, ΔE was deduced by employing E_B of the as-grown film with $x = 0.0$ as a reference. Both ΔE values for Zn 2p and O 1s increased with increasing E_g, implying that increasing ΔE accompanies the widening of E_g. It is interesting to note that ΔE values of the two core level peaks are not identical to each other. Note that the shift of Zn 2p (ΔE_{Zn}) and O 1s (ΔE_O) was ~0.7 eV and ~0.4 eV, respectively, for the as-grown films with $x = 0.47$. ΔE_{Zn} with ~0.7 eV was in good agreement with the increase of E_g as a function of x, shown in the inset in Figure 3. We concluded that the changes in E_B of the Zn 2p are due to widening of E_g caused by alloying, with the Fermi level being pinned just below the CBM. All the $(Zn_{1-x}Mg_x)O$ films showed *n*-type conductivity even when x reached 0.47, indicating that the valence band maximum (VBM) can shift downward with increasing x.

Table 1. MgO Fraction Dependence of the Change in the Full Width at Half-Maximum (fwhm) of the Zn 2p and O 1s Peaks

$\Delta\omega$	$x = 0.0$	$x = 0.07$	$x = 0.47$
Zn 2p	1.31(7)	1.32(4)	1.42(9)
O 1s	1.05(2)	1.05(8)	1.33(7)

An interesting question arises as to why ΔE_O due to alloying was less than ΔE_{Zn}. To resolve this question, we first consider the change in the full width at half-maximum (fwhm, $\Delta\omega$) of the O 1s peaks. It appears that $\Delta\omega$ of the main O 1s peak increases as x increases. Table 1 summarizes the values of $\Delta\omega$ in the Zn 2p and O 1s peaks at $x = 0.0$, 0.07, and 0.47, respectively. Looking first at $\Delta\omega$ in the Zn 2p peak ($\Delta\omega_{Zn}$), negligible change was found in $\Delta\omega_{Zn}$, which was nearly invariant with x. This result means that alloying ZnO with MgO can induce a shift of the Zn 2p peak due to widening of E_g; however, the electronic state of the Zn ion was homogeneous even after alloying. In contrast, remarkably, $\Delta\omega$ in the O 1s main peak ($\Delta\omega_O$) increased, depending on x. $\Delta\omega_O$ at $x = 0.07$ was nearly equal to that at $x = 0.0$, while that at $x = 0.47$ exhibited a larger value (~0.3 eV) than the others. This indicates that Mg substitution for Zn sites is responsible for the change in $\Delta\omega_O$ for the O 1s peaks.

There are several possible reasons for the broadening and shifting of the PES peaks. Band bending at the surface is one of the possibilities. If this is the case, both the Zn 2p and O 1s peak should show broadening and shifting in the same manner. Since the broadening was found only in the O 1s peak, band bending at the surface is not an appropriate explanation for the present results. We will discuss the origin of why only $\Delta\omega_O$ increased and ΔE_O is smaller than ΔE_{Zn} as x increases, with our DFT calculation results, as described below.

Figure 4 shows the lattice parameters of the supercell models predicted by structural optimization using the DFT theory as a function of x in the model. The difference between the observed and the calculated lattice parameters was within a few percent. For example, the calculated values were $a = 0.32540$ nm and $c = 0.52546$ nm for pure ZnO, while the experimental values were $a = 0.32507$ and $c = 0.52083$ nm.[37] Here, we show only the results obtained by

(36) Erhart, P.; Klein, A.; Albe, K. *Phys. Rev. B* **2005**, *72*, 085213.

(37) Abrahams, S. C.; Bernstein, J. L. *Acta Crystallogr., Sect. B* **1969**, *25*, 1233.

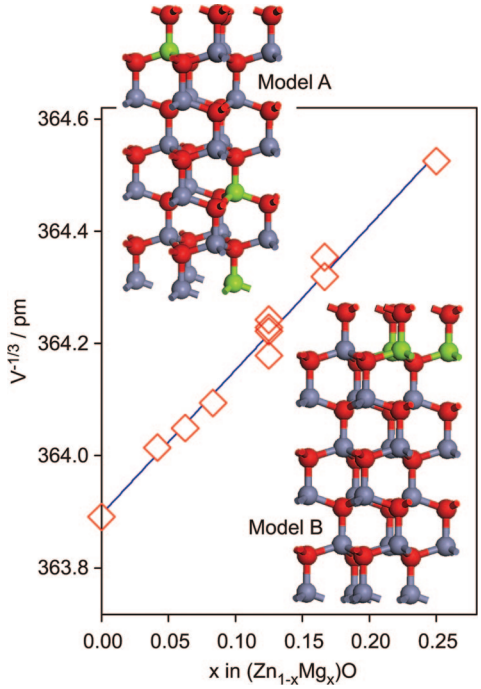

Figure 4. MgO fraction dependence of the optimized unit-cell volume of the supercell. The inset shows two typical superlattice models for $x = 0.125$. Green, red, and gray balls in the models indicate atomic positions of Mg, O, and Zn, respectively.

considering *k*-point separation less than 0.5 nm^{-1}. When only the Γ-point was involved in the BZ integration, the calculated lattice parameters showed the deviation from Vegard's law. On the other hand, if many *k*-points, with *k*-point separation less than 0.5 nm^{-1}, were involved in the BZ integration, the calculated lattice parameters systematically changed with the MgO fraction, satisfying Vegard's law as seen in Figure 4. Since the lattice parameters of $(Zn_{1-x}Mg_x)O$ experimentally determined allow Vegard's law, the results calculated using many *k*-points in BZ are likely more reasonable than those calculated with only the Γ-point. From this viewpoint, we used the calculated results obtained by considering *k*-point separation less than 0.5 nm^{-1}.

In Figure 4, there are different results for the same MgO fraction. These different results with the same MgO fraction were obtained by using different superlattice models. The inset of Figure 4 shows two of four types of superlattice models examined for $x = 0.125$. In the superlattice models, the distribution of Mg ions is restricted by virtual symmetry, while the Mg ions in real alloy are randomly distributed. Since the calculated lattice parameters as well as the density of states were not obviously changed with the choice of superlattice models, it is likely that the model having virtual symmetry and calculation conditions employed in this study are appropriate for simulation of alloy structures. Namely, the conclusion described below will not be affected by the choice of the superlattice model.

Figure 5 shows the DOS in the valence band and the O 2s region in a $[Zn_7MgO_8]$ superlattice. For this case, 15 *k*-points were involved in the BZ integration according to the *k*-point dependence of the optimized structure as described above. In Figure 5, the L-DOS profiles at two O sites are shown in Figure 5b,c, where all of these DOS profiles are separated into the s, p, and d state, together with the

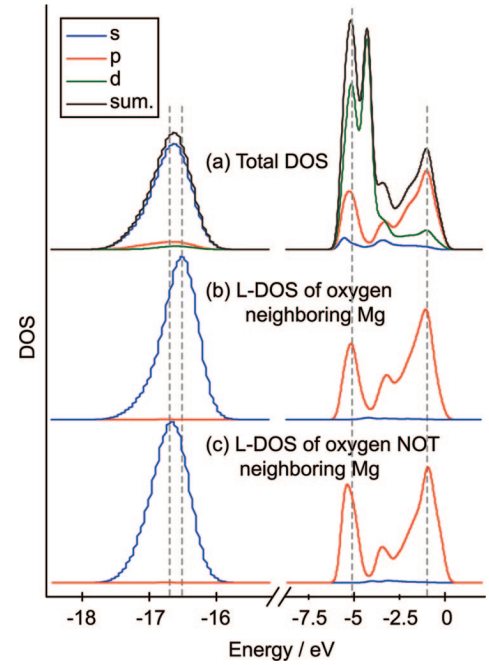

Figure 5. Total (a) and local (b, c) density of states (DOS) in the valence band and O 2s level calculated for a superlattice model of $[Zn_7MgO_8]$.

Table 2. Negative Charge Analysis of an O Ion in Zn_4O and Zn_3MgO Coordination Based on DFT Calculation

coordination	charge of O ion, e
Zn_4O	−0.82
Zn_3MgO	−0.95

total DOS in Figure 5a. We refer to the two O sites to compare the L-DOS of O ions; one is an O ion to which an adjacent Mg ion binds and the other is that relatively far from the Mg ion. In Figure 5, we found that the O 2s level of the O ion neighboring a Mg ion was relatively shallow in comparison with the other O relatively far from a Mg ion. Due to the variation of the chemical state of the O ions, the total DOS of the superlattice was slightly broadened compared to that for pure ZnO (not shown). Table 2 shows the results of Mulliken charge analyses. It was absolutely consistent with the results of L-DOS calculation, presumably because an O ion neighboring a Mg ion was more negatively charged than other O ions. An interesting feature of these results is that an ionic charge of O not neighboring a Mg ion was nearly the same as that of O in pure ZnO, revealing that only an O ion neighboring a Mg ion had extraordinary electronics states, that is, high ionicity indicated by the Mulliken charge analyses.

Note that the DOS of ZnO calculated by the GGA approach does not agree exactly with the results of HX-PES. The electronic state mostly composed of the Zn 3d state, for example, was calculated to be at ∼6 eV below VBM but was found to be at ∼10.8 eV below VBM in the observed valence band spectra. It has been pointed out that the consideration of correlation potential (U) reduces the difference between the theoretical and experimental band diagrams.[38] Thus, it is incorrect to compare the calculated results directly with the observed PES. However, we assume

(38) Janotti, A.; Van de Walle, C. G. *Phys. Rev. B* **2007**, *76*, 165202.

that the DFT results are still indicative of the consideration for semiquantitative electronic state analyses.

As mentioned above, two interesting results from HX-PES are still in question: the first is that ΔE_O due to alloying was less than ΔE_{Zn} and the other is that only oxygen related peaks were broadened by alloying. To answer this question, we compare the HX-PES results with the calculated L-DOS in a superlattice model. This comparison is reasonably certified by our observation of O 1s and O 2s variations with variation of x. Both the O 1s and the O 2s spectra were recognized to show parallel variation in terms of shifting and broadening in the present experiments. We believe this is the reasonable strategy since experimentally the signal-to-noise ratio of O 1s is much higher than that of O 2s and thus more advantageous in the line shape analysis, whereas theoretically O 1s state calculation is far beyond the limitation of the method we adopted.

Taking both the results of the HX-PES and the DFT calculations, we can assume that two kinds of O exist in the $(Zn_{1-x}Mg_x)O$ alloy. According to the DFT calculation summarized in Table 2, the electronic state of an O ion in the $(Zn_{1-x}Mg_x)O$ alloy seems to be affected by a Mg ion with a Mg−O bond, indicative of more negative charge. An O ion with more negative charge likely gives rise to a peak shift to the lower E_B side, corresponding to a smaller shift of the O 1s peak than that of Zn 2p in $(Zn_{1-x}Mg_x)O$. Hence, we can conclude that the E_B shift of the O 1s peak can be explained by both the chemical shift due to the change in the ionicity and the expansion of the bandgap energy, in good agreement with the smaller E_B shift compared to the Zn 2p.

In addition to the higher ionicity of O bound to an adjacent Mg ion, we can discuss the distribution of the wave functions through the DFT calculation. Figure 6 shows that the density distribution constitutes O 2s electrons in a $(Zn_{1-x}Mg_x)O$ superlattice model. Indeed, as compared in Figure 6, an electron orbital, mostly composed of the O 2s state of an O ion neighboring a Mg ion in Figure 6a, was highly localized at the $[MgO_4]$ tetrahedron, corresponding to the DOS with less binding energy. In contrast to the localized Mg−O bond, the other O 2s orbitals situated far from a Mg ion in Figure 6b were found to hybridize and give average spatial distribution at O sites in the lattice. This illuminates the fact that the electronic state of an O ion originating from Mg substitution for the Zn site was highly localized at the $[MgO_4]$ tetrahedron, thereby giving rise to broadening of $\Delta\omega_O$ when too high MgO fraction is incorporated in the ZnO lattice, as shown in Figure 2 and Table 1.

It is of crucial importance to understand the electronic structures of $(Zn_{1-x}Mg_x)O$ widegap semiconductors, for valence control and device applications based on ZnO materials. Moreover, it has been required to elucidate the band diagram of $(Zn_{1-x}Mg_x)O$ to fabricate high-performance heterojunction devices. To this end, we draw the band diagrams of ZnO and $(Zn_{1-x}Mg_x)O$ from the HX-PES results, and we focus on how the MgO fraction affects the variations in the band diagram. To illustrate the band offset for $(Zn_{1-x}Mg_x)O$ alloys, we employed VBM energy relative to the Fermi level determined by HX-PES and E_g deduced from optical transmittance measurements as mentioned above.

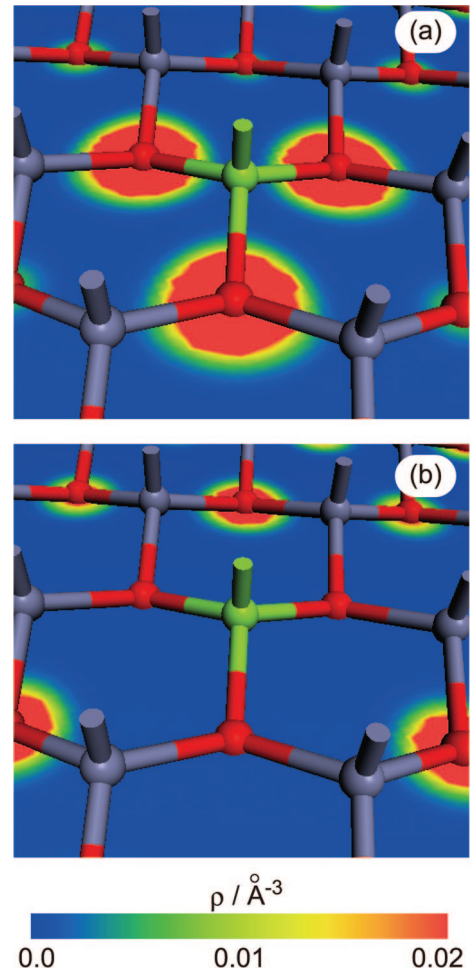

Figure 6. Electron density distributions of electron orbitals in a superlattice model of $[Zn_{47}MgO_{48}]$. A typical orbital composed of an O 2s electron of four O ions bonding with a Mg ion (a) and another one composed of O 2s electrons of O ions not bonding with Mg ions (b). Green, red, and gray balls indicate atomic positions of Mg, O, and Zn, respectively.

Here, energies at VBM relative to the Fermi level were determined by the linear extrapolation of the valence band spectra near the onset of the O 2p bands in $(Zn_{1-x}Mg_x)O$. Note that the shift in VBM evaluated by this way was parallel with that of the Zn 2p peak.

Figure 7 illustrates the band diagrams for (a) $x = 0.07$ and (b) 0.47 in $(Zn_{1-x}Mg_x)O$, along with that for $x = 0.0$. This figure clearly indicates that the VBM level relative to E_F lowered with the increase of x, and the magnitude of the shift of VBM was parallel with the expansion of E_g with increasing x. This also means that the CBM level relative to E_F was not remarkably changed with x. Actually, the CBM energy relative to E_F, calculated by subtracting the VBM energy relative to E_F from E_g, was in the range 0.04−0.08 eV, and these values were much smaller than the change in VBM energy with x. As a result, we realized that E_F was situated close to the CBM in all the samples regardless of x. These results directly indicate the difficulty to fabricate p-type $(Zn_{1-x}Mg_x)O$. Figure 7 implies that E_F is pinned nearby CBM even in nominally undoped $(Zn_{1-x}Mg_x)O$, indicating that the native defects and/or unintentional impurities causing n-type conduction must be eliminated to achieve successful hole doping into $(Zn_{1-x}Mg_x)O$. In contrast, the results shown in Figure 7 are good news for the people seeking for electric

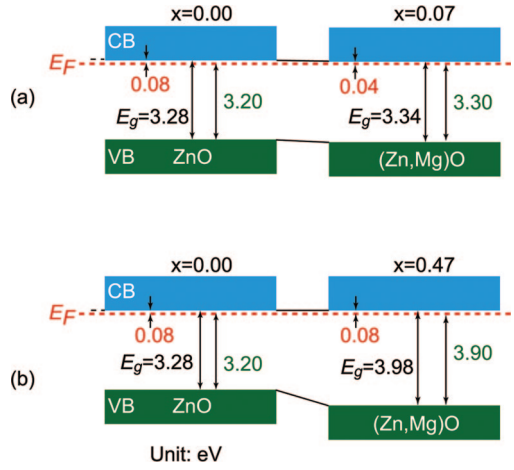

Figure 7. Energy diagram of $(Zn_{1-x}Mg_x)O$ films with $x = 0.07$ (a) and 0.47 (b), indicating the optical energy bandgap (E_g) and the energy difference between the CMB and the Fermi level and between the E_F and VBM energy.

conductor having transparency to UV light. Figure 7 means that shallow donors can exist in $(Zn_{1-x}Mg_x)O$ with high x, and these results encourage us to develop transparent conducting $(Zn_{1-x}Mg_x)O$ with E_g greater than 4 eV.

Conclusions

We have carefully examined the electronic structures of PLD-grown $(Zn_{1-x}Mg_x)O$ alloy semiconductors using HX-PES and DFT calculations. The E_B values in the core-level peaks of Zn 2p and O 1s were found to be shifted to the higher E_B side, which strongly depended on x and accompanied the resulting increase in E_g. The shift of the O 1s peak was less than that observed in Zn 2p because of the enhanced ionicity of O ions as a result of adding Mg ions to form the $(Zn_{1-x}Mg_x)O$ alloy. The DFT calculations suggest that an O ion bonding with a Mg ion has a higher negative charge compared to that not bonding with a Mg ion, thus yielding a negative shift in L-DOS of the O 2s, in agreement with PES results. The O orbital with the Mg−O bond is likely to be highly localized at the $[MgO_4]$ tetrahedron and corresponds to the appearance of the structure in the DOS with shallower binding energy. Finally, we illustrate the band diagram of $(Zn_{1-x}Mg_x)O$ based on the results of optical and valence band spectra, revealing the fact that the Fermi level is close to the bottom of the conduction band even for $x = 0.47$.

Acknowledgment. This study was carried out with support from a Grant-in-Aid for the World Premier Research Institute Initiative promoted by the Ministry of Education, Culture, Sports, Science, and Technology (MEXT), Japan. The HX-PES measurements were performed under the approval of the NIMS Beamline Station (Proposal No. 2006B4604 and 2007A4609). The authors are grateful to HiSOR, Hiroshima University, and JAEA/SPring-8 for the development of HX-PES at BL15XU of SPring-8. This study was also partially supported by a Grant-in-Aid for Scientific Research from the Japan Society for Promotion of Science and MEXT, Japan. Dr. Koyama of the National Institute of Advanced Industrial Science and Technology (AIST), Japan, is also acknowledged for his kind introduction to the first principle DFT calculation using the pseudopotential technique.

CM802467N